

## CHANDRA OBSERVATIONS OF EIGHT SOURCES DISCOVERED BY INTEGRAL

JOHN A. TOMSICK<sup>1</sup>, ROMAN KRIVONOS<sup>2</sup>, QINAN WANG<sup>1</sup>, ARASH BODAGHEE<sup>3</sup>, SYLVAIN CHATY<sup>4,5</sup>, FARID RAHOUI<sup>6,7</sup>, JEROME RODRIGUEZ<sup>4</sup>, FRANCESCA M. FORNASINI<sup>1,8</sup>

Accepted by ApJ

### ABSTRACT

We report on 0.3–10 keV observations with the *Chandra X-ray Observatory* of eight hard X-ray sources discovered within 8° of the Galactic plane by the *INTEGRAL* satellite. The short (~5 ks) *Chandra* observations of the IGR source fields have yielded very likely identifications of X-ray counterparts for three of the IGR sources: IGR J14091–6108, IGR J18088–2741, and IGR J18381–0924. The first two have very hard spectra in the *Chandra* band that can be described by a power-law with photon indices of  $\Gamma = 0.6 \pm 0.4$  and  $-0.7^{+0.4}_{-0.3}$ , respectively (90% confidence errors are given), and both have a unique near-IR counterpart consistent with the *Chandra* position. IGR J14091–6108 also displays a strong iron line and a relatively low X-ray luminosity, and we argue that the most likely source type is a Cataclysmic Variable (CV), although we do not completely rule out the possibility of a High Mass X-ray Binary. IGR J18088–2741 has an optical counterpart with a previously measured 6.84 hr periodicity, which may be the binary orbital period. We also detect five cycles of a possible 800–950 s period in the *Chandra* light curve, which may be the compact object spin period. We suggest that IGR J18088–2741 is also most likely a CV. For IGR J18381–0924, the spectrum is intrinsically softer with  $\Gamma = 1.5^{+0.5}_{-0.4}$ , and it is moderately absorbed,  $N_{\text{H}} = (4 \pm 1) \times 10^{22} \text{ cm}^{-2}$ . There are two near-IR sources consistent with the *Chandra* position, and they are both classified as galaxies, making it likely that IGR J18381–0924 is an Active Galactic Nucleus (AGN). For the other five IGR sources, we provide lists of nearby *Chandra* sources, which may be used along with further observations to identify the correct counterparts, and we discuss the implications of the low inferred *Chandra* count rates for these five sources.

*Subject headings:* galaxies: active — stars: white dwarfs — stars: neutron X-rays: galaxies — X-rays: stars — stars: individual (IGR J14091–6108, IGR J15335–5420, IGR J17164–3803, IGR J17174–2436, IGR J17306–2015, IGR J18088–2741, IGR J18381–0924, IGR J20107+4534)

### 1. INTRODUCTION

The *INTERNATIONAL Gamma-Ray Astrophysics Laboratory* (*INTEGRAL*) satellite (Winkler et al. 2003) has been surveying the sky in the hard X-ray/soft gamma-ray band since its launch in 2002. The Imager on-Board the *INTEGRAL* Satellite (IBIS; Ubertini et al. 2003) has detected large numbers of sources in the 20–100 keV band. The current version of the *INTEGRAL* General Reference Catalog<sup>9</sup> includes 954 sources that have been detected by IBIS, and the majority of these are “IGR” sources, meaning that either they were discovered by *INTEGRAL*, or they were not known to produce hard X-ray emission prior to the *INTEGRAL* detection. The “*INTEGRAL* Sources” website<sup>10</sup> lists over 550 IGR sources. The most recent published IBIS catalogs include Bird et al. (2010), which includes information on more than 700 sources (IGR and

non-IGR), and Krivonos et al. (2012), which lists 402 sources within 17.5° of the Galactic plane<sup>11</sup>.

Thus, the IGR sources represent a large population of proven hard X-ray emitters, but, in most cases, more information is needed to determine their nature. The fact that these sources produce emission above 20 keV indicates that they are sites of particle acceleration or extreme heating, which leads to the production of non-thermal emission. Based on the source type identifications that have been obtained to date, Active Galactic Nuclei (AGN) are the most numerous group of IGR sources, but there are hundreds of Galactic sources as well, including Low Mass X-ray Binaries (LMXBs), High Mass X-ray Binaries (HMXBs), Cataclysmic Variables (CVs), and Pulsar Wind Nebulae (PWNe). *INTEGRAL* discoveries have increased the total number of known HMXBs from 65 to 96 and have multiplied the number of supergiant HMXBs almost threefold from 13 to 36 (Walter et al. 2015). Many of the IGR HMXBs belong to two new classes: the obscured HMXBs, where the compact object is enshrouded in the wind from the companion star (e.g., Matt & Guainazzi 2003; Filliatre & Chaty 2004; Walter et al. 2006); and the Supergiant Fast X-ray Transients (SFXTs; Negueruela et al. 2006; Smith et al. 2006; Pellizza et al. 2006; Sidoli et al. 2013; Romano et al. 2014). There are many other interesting individual Galactic objects such as the LMXB and transitional pulsar IGR J18245–2452 (Papitto et al. 2013), and the high velocity pulsar and PWN IGR J11014–6103 (Pavan et al. 2011; Tomsick et al. 2012b).

Observations with the *Chandra X-ray Observatory* are es-

<sup>1</sup> Space Sciences Laboratory, 7 Gauss Way, University of California, Berkeley, CA 94720-7450, USA

<sup>2</sup> Space Research Institute, Russian Academy of Sciences, Profsoyuznaya 84/32, 117997 Moscow, Russia

<sup>3</sup> Georgia College & State University, CBX 82, Milledgeville, GA 31061, USA

<sup>4</sup> Laboratoire AIM, UMR 7158 CEA/DSM-CNRS-Université Paris Diderot, IRFU/Sap, F-91191 Gif-sur-Yvette Cedex, France

<sup>5</sup> Institut Universitaire de France, 103 Boulevard Saint-Michel, 75005 Paris, France

<sup>6</sup> European Southern Observatory, Karl Schwarzschild-Strasse 2, 85748 Garching bei Munchen, Germany

<sup>7</sup> Department of Astronomy, Harvard University, 60 Garden Street, Cambridge, MA 02138, USA

<sup>8</sup> Astronomy Department, University of California, 601 Campbell Hall, Berkeley, CA 94720, USA

<sup>9</sup> see <http://www.isdc.unige.ch/integral/catalog/39/catalog.html>

<sup>10</sup> see <http://irfu.cea.fr/Sap/IGR-Sources/>

<sup>11</sup> see <http://hea.iki.rssi.ru/integral>

pecially useful for determining the nature of the IGR sources because *Chandra*'s superior angular resolution can improve the source localization from arcminutes (with *INTEGRAL*) to less than an arcsecond; thus, providing the opportunity to identify counterparts at other wavelengths, such as the optical or near-IR where all-sky images and catalogs are readily available. In addition, *Chandra*'s 0.3–10 keV coverage provides constraints on the soft X-ray spectrum, allowing for a determination of column densities, spectral slopes, and, in some cases, emission lines. We have been carrying out *Chandra* programs to follow up IGR sources in several previous *Chandra* observing cycles (Tomsick et al. 2006, 2008, 2009, 2012a; Bodaghee et al. 2012), and other groups also have similar programs (e.g., Fiacchi et al. 2010; Ratti et al. 2010; Paizis et al. 2011, 2012; Nowak et al. 2012; Karasev et al. 2012).

For the *Chandra* cycle 15 program, we selected IGR sources from the Krivonos et al. (2012) catalog. We excluded sources whose classification (e.g., AGN, HMXB, etc.) is known, leaving 34 unclassified sources of which 30 have an IGR designation. Next, we only considered sources situated within  $8^\circ$  of the Galactic Plane, which increases the probability of identifying new X-ray binaries, CVs, and PWNe. This selection also takes advantage of *Chandra*'s unparalleled X-ray positional accuracy, which we require to pinpoint an optical/IR counterpart in these crowded fields. After removing sources with existing soft X-ray coverage with *Chandra* and *XMM-Newton*, we were left with ten sources. We reported on the results of the cycle 15 *Chandra* observations for two of the sources (IGR J04059+5416 and IGR J08297–4250), concluding that they are AGN (Tomsick et al. 2015).

In this paper, we report on the results of the remaining eight observations. Section 2 provides a brief description of the *Chandra* observations and how the data were processed. In Section 3, we present results on *Chandra* source detection and photometry. For the three *Chandra* sources that we identify with IGR sources, we present *Chandra* and *INTEGRAL* energy spectra, *Chandra* light curves, and IR source identifications. A discussion of the nature of the three sources is included in Section 4, and conclusions are presented in Section 5. In addition, we include an Appendix with a full listing of the *Chandra* sources detected.

## 2. CHANDRA OBSERVATIONS AND DATA PROCESSING

Information about the eight *Chandra* observations, which occurred between late-2013 and early-2015, is given in Table 1. The integration time for each observation is  $\sim 5$  ks, and we used the Advanced CCD Imaging Spectrometer (ACIS-I) instrument (Garmire et al. 2003). The pointing position was at the best known source position, and, in seven cases, this corresponds to the position measured by *INTEGRAL* (Krivonos et al. 2012). For IGR J14091–6108, a likely *Swift* counterpart has been reported (Landi et al. 2012), and we used the *Swift* position for the *Chandra* pointing. After obtaining the data from the *Chandra* X-ray Center, all of the *Chandra* data reduction in this work was done using the *Chandra* Interactive Analysis of Observations (CIAO) version 4.7 software and Calibration Data Base (CALDB) 4.6.7. We made new event lists using `chandra_repro` and used these event lists for the analysis described below.

## 3. ANALYSIS AND RESULTS

### 3.1. *Chandra* Source Detection and Photometry

For each of the eight observations, we inspected the full field of view (ACIS-I and ACIS-S) and used `wavdetect` (Freeman et al. 2002) to search for *Chandra* sources over ACIS-I, on which the *INTEGRAL* source position falls in each case. The accuracy of the *INTEGRAL* positions is  $2'.1$  at 68% confidence (Krivonos et al. 2012), indicating that it is very likely that the true source position lies in the  $16'.9$ -by- $16'.9$  ACIS-I field of view. In order to detect sources in both soft and hard bands, we divided events into a soft band with energy between 0.3 keV and 2 keV, and a hard band with energy between 2 keV and 10 keV. Before we ran `wavdetect`, we used `fluximage` and `mkpsfmap` to generate the exposure map and the point spread function (PSF) map in order to improve the accuracy of detection. A small number of sources with one or two counts was detected, and we discarded these. In total, we detected 115 sources in the ACIS-I fields of view, with the most and least crowded fields having 29 and 7 sources, respectively (see Table 1 for the totals in each field). Tables listing the basic information (position, counts detected, and hardness) for all 115 sources, as well as more details on how we obtained this information, are provided in the Appendix.

For all 115 sources, we performed photometry to determine the number of source counts in the 0.3–10 keV, 0.3–2 keV, and 2–10 keV bands. The size of the *Chandra* PSF changes significantly over the field of view, and we determined the off-axis angle for each source and then used the *Chandra* PSF Viewer<sup>12</sup> to determine the radius of the 90% encircled counts fraction at 3 keV for each source. For the photometry, we extracted counts from circular regions that were twice this radius, so that the extraction regions enclosed more than 99% of the counts. For each field, we identified a large source-free region, and used this region to estimate and then subtract the background contribution within each source extraction region. The results of the photometry are shown by plotting the hardness of each source, which is defined as  $(C_2 - C_1)/(C_2 + C_1)$ , where  $C_2$  is the number of counts in the 2–10 keV band and  $C_1$  is the number of counts in the 0.3–2 keV band, vs. the intensity, which is the number of counts in the 0.3–10 keV band (Figure 1).

Three sources stand out from the rest of the sources in the hardness-intensity diagram: CXOU J140846.0–610754 in the field of IGR J14091–6108; CXOU J180839.8–274131 in the field of IGR J18088–2741; and CXOU J183818.5–092552 in the field of IGR J18381–0924. CXOU J140846.0–610754 has 404.9 counts, a hardness of  $0.56 \pm 0.06$ , and it is only  $0'.45$  from the center of the error circle, which is well within the  $1\text{-}\sigma$  *INTEGRAL* error circle. CXOU J180839.8–274131 has 229.9 counts and a hardness of  $0.76 \pm 0.09$ . While it is  $4'.5$  from the center of the *INTEGRAL* error circle, it is an order of magnitude brighter than any source that is closer to the *INTEGRAL* position, and it is harder than any other source in the field with more than 10 counts. CXOU J183818.5–092552 has 302.7 counts, a hardness of  $0.73 \pm 0.08$ , and it is  $2'.8$  from the best *INTEGRAL* position, which is within the  $2\text{-}\sigma$  error circle. Thus, these three *Chandra* sources are very likely counterparts to their respective *INTEGRAL* sources, and in the following sections, we report on the details of these three sources, including their *Chandra* and *INTEGRAL* energy spectra, their *Chandra* light curves, and whether their *Chandra* positions allow us to identify counterparts at other wavelengths.

<sup>12</sup> see [http://cxc.cfa.harvard.edu/cgi-bin/prop\\_viewer/build\\_viewer.cgi?psf](http://cxc.cfa.harvard.edu/cgi-bin/prop_viewer/build_viewer.cgi?psf)

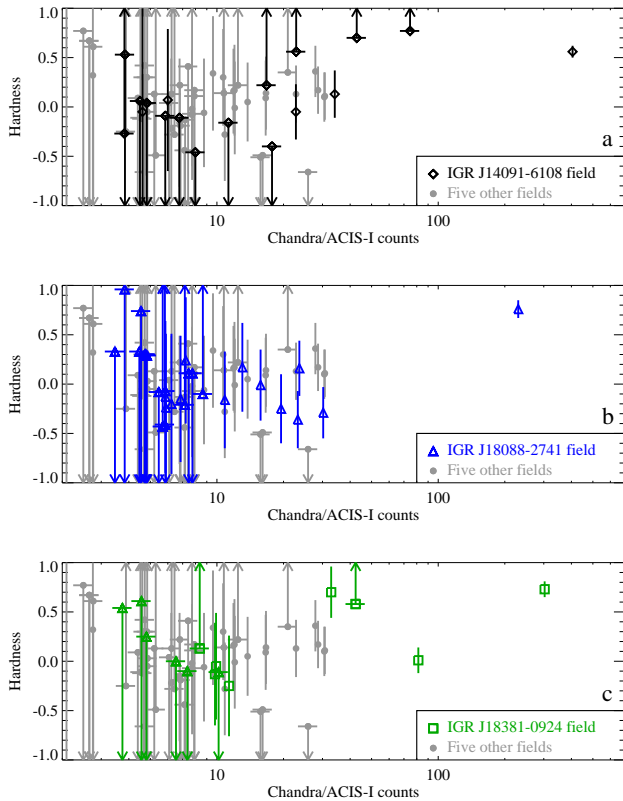


FIG. 1.— Hardness-intensity diagrams, where the intensity is given as the number of ACIS-I counts in the 0.3–10 keV energy band. The hardness is given by  $(C_2 - C_1)/(C_2 + C_1)$ , where  $C_2$  is the number of counts in the 2–10 keV band and  $C_1$  is the number of counts in the 0.3–2 keV band. The black diamonds in (a), blue triangles in (b), and green squares in (c) correspond to sources in the IGR J14091–6108, IGR J18088–2741, and IGR J18381–0924 fields, respectively. The points in the other fields are shown in grey.

For the other five IGR fields, some of the *Chandra* sources detected are potential counterparts. However, in those cases, there is a significant probability that the association is spurious. We first focus on CXOU J140846.0–610754, CXOU J180839.8–274131, and CXOU J183818.5–092552 and then consider the upper limits for the other five fields.

### 3.2. *Chandra* and *INTEGRAL* Energy Spectra

For all three sources, we produced *Chandra* and *INTEGRAL* energy spectra. For *Chandra*, we used circular source extraction regions with the same radii used for the photometry:  $2.''5$  for CXOU J140846.0–610754 and CXOU J183818.5–092552; and  $5.''0$  for CXOU J180839.8–274131. However, as CXOU J140846.0–610754 was on-axis with an ACIS count rate of 0.08 c/s, the spectrum can be distorted by photon pile-up. Using the Portable, Interactive Multi-Mission Simulator (PIMMS)<sup>13</sup>, we estimate the pile-up level at 10%. Thus, for CXOU J140846.0–610754, we used an annular source region with an inner radius of  $0.''5$  and an outer radius of  $2.''5$ . In all three cases, a background spectrum was obtained from a source-free region close to the source. The source and background spectra and the response matrices were produced with the `specextract` script. We included the 0.3–10 keV energy range, and rebinned each spectrum with the criterion that the source be detected at a signal-to-noise (S/N) level of 3 or greater in each bin (except for the

highest energy bin).

The *INTEGRAL* energy spectra were produced using publicly available data from the IBIS/ISGRI instrument over a time period from 2003 to the end of 2014, yielding effective exposure times<sup>14</sup> of 5.0, 23.6, and 8.0 Ms for IGR J14091–6108, IGR J18088–2741, and IGR J18381–0924, respectively. We reduced the IBIS/ISGRI data with the *INTEGRAL* data analysis package developed at IKI RAN<sup>15</sup> (see, e.g., Churazov et al. 2005; Krivonos et al. 2010; Churazov et al. 2014, and references therein) using the most up-to-date gain calibration for ISGRI (Caballero et al. 2013) available through the Offline Scientific Analysis (OSA) version 10.1, provided by the ISDC<sup>16</sup>. To take the ongoing detector degradation and loss of sensitivity at low energies (Caballero et al. 2013) into account, we adjusted the flux scale in each IBIS sky image using the flux of the Crab nebula measured in the observation that is closest in time to when the data for the sky image was obtained. This results in a smooth recalibration of the ancillary response function over the span of the observations from 2003 to 2014. We previously used the same procedure for a subset of the data as described in Krivonos et al. (2012). The energy spectra were obtained from sky mosaic images in four energy bands: 17–26 keV, 26–38 keV, 38–57 keV, and 57–86 keV. The corresponding energy response matrices were produced using Crab nebula observations, assuming a spectral shape of  $10(E/1\text{keV})^{-2.1}$  photons  $\text{cm}^{-2} \text{s}^{-1} \text{keV}^{-1}$ .

For each source, we initially fit the *Chandra* and *INTEGRAL* spectra separately. The S/N = 3 binning for *Chandra* results in about 10 counts per bin, which is close to the Poisson regime. Thus, for the *Chandra*-only fits, the fitting was done by minimizing the Cash statistic (Cash 1979). Due to the high *INTEGRAL* background, we performed the fits to the *INTEGRAL* spectra and the fits to the joint *Chandra*+*INTEGRAL* spectra by minimizing the  $\chi^2$  statistic. The fit parameters and  $\chi^2$  values are reported in Table 2, and the folded and unfolded spectra are shown in Figure 2. The errors on the spectral parameters in the table as well as values quoted in this section are at the 90% confidence level.

For CXOU J140846.0–610754, an absorbed power-law model to the *Chandra* spectrum leaves residuals in the iron line region, and we find that the addition of a Gaussian iron line at  $E_{\text{line}} = 6.6 \pm 0.2$  keV with a width of  $\sigma_{\text{line}} < 0.6$  keV leads to an improvement in the Cash statistic from 32.6 for 22 degrees of freedom (dof) to 19.4 for 19 dof. We used `simfittest` to produce 10,000 simulated *Chandra* spectra with the absorbed power-law model, fit the spectra with and without the addition of a Gaussian with  $E_{\text{line}}$  between 6.4 and 7.1 keV and  $\sigma_{\text{line}} < 0.6$  keV, and recorded the Cash statistics for all the fits. Out of the 10,000 spectra, an improvement in the Cash statistic of 13.2 (=32.6–19.4) or more was seen eight times, corresponding to a detection significance of  $3.35\text{-}\sigma$ . Thus, we included this line, which has an equivalent width (EW) of  $1.2^{+0.9}_{-0.7}$  keV, in our subsequent fits. Some weak residuals remain near 4.0 keV, but adding a Gaussian leads to only a small reduction in the Cash statistic to 15.0 for 16 dof. Using `simfittest`, there is a 15% probability of obtaining such an improvement by chance, indicating that the 4 keV feature is not statistically significant.

<sup>14</sup> These correspond to dead-time corrected exposure times calculated for the fully coded field of view.

<sup>15</sup> Space Research Institute of the Russian Academy of Sciences, Moscow, Russia

<sup>16</sup> INTEGRAL Data Center for Astrophysics, <http://www.isdc.unige.ch/>

<sup>13</sup> see <http://asc.harvard.edu/toolkit/pimms.jsp>

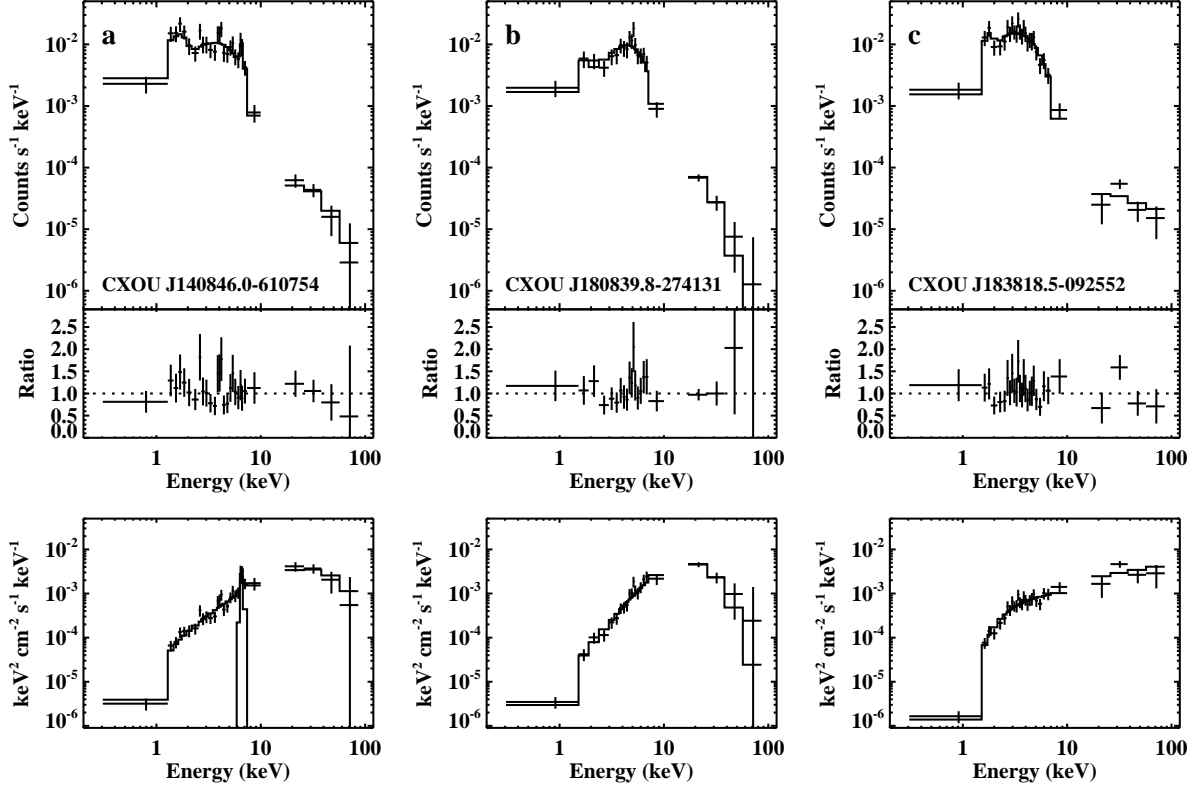


FIG. 2.— *Chandra* and *INTEGRAL* energy spectra for (a) CXOU J140846.0–610754/IGR J14091–6108, (b) CXOU J180839.8–274131/IGR J18088–2741, and (c) CXOU J183818.5–092552/IGR J18381–0924. For each source, the top panel is the counts “folded” spectrum, the middle panel is the data-to-model ratio, and the bottom panel is the “unfolded” spectrum in flux units. From left to right, the models are: `tbabs*(gaussian+cutoffpl)`, `tbabs*cutoffpl`, and `tbabs*powerlaw`.

As reported in Table 2, with *Chandra*, we measure a column density of  $(1.0^{+0.7}_{-0.6}) \times 10^{22} \text{ cm}^{-2}$  and a power-law photon index of  $\Gamma = 0.6 \pm 0.4$  for CXOU J140846.0–610754. This indicates that the spectrum in the 0.3–10 keV bandpass is even harder than the previously reported *Swift* value of  $\Gamma \sim 1.3$  (Landi et al. 2012). While the photon index measured by *Chandra* is very hard, a power-law fit to the *INTEGRAL* spectrum yields a much softer photon index of  $\Gamma = 2.9^{+1.0}_{-0.7}$ , indicating that there must be a break or a cutoff between the *Chandra* and *INTEGRAL* spectra. To fit the *Chandra* and *INTEGRAL* spectra together, we used the model `cutoffpl`, which is a power-law multiplied by an exponential,  $e^{-E/E_{\text{fold}}}$ . As the *Chandra* and *INTEGRAL* observations were made at different times, and the source might be variable, we originally allowed for a normalization difference between the two spectra, obtaining  $N_{\text{INTEGRAL}}/N_{\text{Chandra}} = 1.8^{+2.8}_{-1.1}$ . Table 2 shows that the changes in the parameters are not significant when we fix the normalization ratio to 1.0. With the ratio fixed to 1.0, we find  $\Gamma = 0.1^{+0.4}_{-0.5}$ , and  $E_{\text{fold}} = 14^{+11}_{-5} \text{ keV}$ , and the folded and unfolded spectra are shown in Figure 2. For these fits, we restricted  $\sigma_{\text{line}}$  to be less than 0.6 keV.

We performed similar spectral fits for CXOU J180839.8–274131, and the results are reported in Table 2. While the *Chandra* power-law index is  $\Gamma = -0.7^{+0.4}_{-0.3}$ , fitting the *INTEGRAL* spectrum separately gives  $\Gamma = 3.8^{+1.2}_{-0.8}$ . As the *Chandra* source is 4.8′ off-axis, and the ACIS count rate is lower than for CXOU J140846.0–610754, 0.05 c/s, photon pile-up is not a concern, indicating that the spectrum is very hard in the 0.3–10 keV band and has a strong cutoff at higher

energies. Fitting the *Chandra* and *INTEGRAL* spectra with a `cutoffpl` model and the normalization ratio free gives  $N_{\text{INTEGRAL}}/N_{\text{Chandra}} = 0.8^{+0.6}_{-0.4}$ . With the normalization fixed to 1.0, we find  $\Gamma = -1.5^{+0.4}_{-0.2}$  and  $E_{\text{fold}} = 4.8^{+1.1}_{-0.8} \text{ keV}$ . We also find that the spectrum is not highly absorbed with  $N_{\text{H}} < 7 \times 10^{21} \text{ cm}^{-2}$ .

The CXOU J183818.5–092552 spectrum is different from the previous two sources in that the power-law slopes measured by *Chandra* ( $\Gamma = 1.5^{+0.5}_{-0.4}$ ) and *INTEGRAL* ( $\Gamma = 1.8 \pm 0.6$ ) are consistent with each other. Fitting the *Chandra* and *INTEGRAL* spectra together gives a normalization ratio of  $N_{\text{INTEGRAL}}/N_{\text{Chandra}} = 1.6^{+2.1}_{-0.9}$ . With the normalization ratio fixed to 1.0, we find  $\Gamma = 1.4 \pm 0.1$ , and no cutoff is required (see Figure 2). This source also differs from the other two in that it is moderately absorbed with  $N_{\text{H}} = (3.8^{+0.9}_{-0.7}) \times 10^{22} \text{ cm}^{-2}$ .

### 3.3. *Chandra* Light Curves

For the three *Chandra* sources associated with *INTEGRAL* sources, we made 0.3–10 keV light curves with 200 s time bins (Figure 3). We performed two tests to check the sources for variability: a Kolmogorov-Smirnov (KS) test and a  $\chi^2$  test. The KS test is good for low count rates because it compares the event arrival times to a constant reference distribution and does not require the data to be binned. While the KS test is sensitive to random variations, like bursts, it is not as good at finding periodic variability. Thus, we also perform a  $\chi^2$  test by fitting a constant function to the binned light curves. Although this test is problematic in low count situations where the time bins follow a Poisson rather than a Gaussian distribu-

tion, in our case, we typically have 10–20 counts per bin, and  $\chi^2$  statistics are a good approximation.

For CXOU J140846.0–610754, the KS test measures only a 1.2% probability that the source is constant. The  $\chi^2$  test also indicates that the source is very likely to be variable as the reduced  $\chi^2$  is 2.1 for 25 dof. Although the light curve for CXOU J180839.8–274131 appears to be even more variable, the KS test probability is higher, 2.2%. However, the fit to the binned light curve with a constant gives a reduced  $\chi^2$  of 4.1 for 25 dof, confirming that there is a high level of variability. For the third source, CXOU J183818.5–092552, the KS test probability is 8.5%, which does not indicate significant variability. This is confirmed by the second test since we find a reduced  $\chi^2$  of 1.0 for 25 dof.

As CXOU J140846.0–610754 and CXOU J180839.8–274131 show evidence for variability, we performed light curve folding on many trial periods to determine if there is evidence for periodic variability. For each trial period, the  $\chi^2$  for a fit with a constant function is calculated, and a large value of  $\chi^2$  can indicate periodic variability. Although the former source did not show any candidate periods, CXOU J180839.8–274131 exhibits a broad and strong  $\chi^2$  peak between 800 s and 950 s (Figure 4). Although we note that the entire duration of our observation only covers five periods of the candidate oscillation, the folded light curve (Figure 4) shows that if the signal is real, it has a very large amplitude (defined as maximum minus minimum divided by maximum plus minimum) of  $\approx 80\%$ .

#### 3.4. IR Identifications

The fields of CXOU J140846.0–610754 and CXOU J180839.8–274131 were covered by the VISTA Variables in the Via Lactea (VVV) survey (Minniti et al. 2010), and the field of CXOU J183818.5–092552 was covered by the UKIRT Infrared Deep Sky Survey (UKIDSS) survey (Lawrence et al. 2007). We used the images from these surveys to identify possible near-IR counterparts. Figure 5a shows the  $K_s$ -band images with the *Chandra* positions. For CXOU J140846.0–610754, we confirm the association with VISTA source 515845105705 (VVV J140845.99–610754.1) reported in Tomsick et al. (2014), and we provide the VISTA  $Z$ -,  $Y$ -,  $J$ -,  $H$ -, and  $K_s$ -magnitudes in Table 3. As reported in Tomsick et al. (2014), this source is also listed in the *Spitzer*/GLIMPSE catalog as G312.1289+00.3516.

CXOU J180839.8–274131 is within  $0.''41$  of the VISTA source VVV J180839.77–274131.7, and the  $K_s$ -band image shown in Figure 5b indicates that this is the only possible counterpart in the VVV images. The VISTA magnitudes for this counterpart are given in Table 3. We also used the Vizier website to search for possible counterparts of this source in other catalogs, and we find a match with OGLE-BLG-RRLYR-14363, which is source number 14363 in the Optical Gravitational Lensing Experiment (OGLE-III) Catalog of Variable Stars (Soszyński et al. 2011). The OGLE-III catalog indicates that the star varies periodically in the  $I$ -band with a period of  $0.28494563 \pm 0.00000062$  days. We obtained the  $I$ -band measurements folded on this period, and the folded light curve is shown in Figure 6. While Soszyński et al. (2011) classify this source as an RR Lyrae star, a remark in the catalog indicates that the classification is uncertain, and we discuss this further in Section 4.

The position of CXOU J183818.5–092552 is consistent with two near-IR sources from the UKIDSS Galactic Plane

Survey (UGPS): UGPS J183818.59–092551.8 at an angular distance of  $0.''47$  and UGPS J183818.58–092552.9 at an angular distance of  $0.''73$ . Based on their spatial profiles in the near-IR, both sources are classified as galaxies in the UGPS catalog. The probability that the sources are stellar (i.e., not extended) is  $<1\%$  for UGPS J183818.59–092551.8 and  $5\%$  for UGPS J183818.58–092552.9. In the UGPS catalog, the magnitudes listed for these sources do not appear to match the image shown in Figure 5c. Specifically, in the images, the source to the south (UGPS J183818.58–092552.9) is clearly the brighter of the two, but the catalog lists it as  $K = 13.040 \pm 0.003$  (UKIDSS data release 10) compared to  $K = 12.822 \pm 0.002$  for the northern source (UGPS J183818.59–092551.8). The UGPS survey has  $K$ -band images taken on 2005 September 28 and nearly three years later on 2008 May 31, and we examined both of the images to look for source variability; however, there are no discernible differences between the two images. The UKIDSS photometry is carried out using  $2''$  radius extraction regions, and we suspect that this does not yield correct results for these two sources, which have a separation of  $\approx 1''$ . We note that UGPS J183818.59–092551.8 appears to be approximately the same brightness as the two sources to the south of the blended pair, and these are both listed as having  $K = 14.2$  in the UKIDSS catalog. Thus, we conclude that the true brightnesses of UGPS J183818.59–092551.8 and UGPS J183818.58–092552.9 are likely  $K \approx 14$  and  $K \approx 13$ , respectively (Table 3). The *Chandra* position is compatible with both sources, and both remain as candidate counterparts to CXOU J183818.5–092552.

#### 3.5. Upper Limits for the Other Five IGR Sources

For IGR J15335–5420, IGR J17164–3803, IGR J17174–2436, IGR J17306–2015, and IGR J20107+4534, none of the *Chandra* sources listed in the table in the Appendix are clear counterparts, but these sources are possible counterparts. We identified the highest count rate source in each field and took this as the upper limit on the *Chandra* count rate. Then, extrapolating using a power-law model and the ACIS response matrix, we compared the *Chandra* count rate upper limit to the actual flux measurement for each of the five sources reported in Krivonos et al. (2012). There are at least three reasons why the sources might be relatively faint in the *Chandra* energy band: 1. the source may be intrinsically hard; 2. the source may be highly absorbed; or 3. the source may be variable (and any combination of these three is also possible). Table 4 lists the *Chandra* count rate upper limit and the 17–60 keV flux measured by *INTEGRAL* (Krivonos et al. 2012). Then, we performed calculations to consider the three effects mentioned above. In the first calculation, we determined the values of  $\Gamma$  required to produce the low *Chandra* count rate if the sources are unabsorbed. Second, we assumed a value of  $\Gamma = 2.1$ , which is used in Krivonos et al. (2012) to determine the *INTEGRAL* fluxes, and calculated the column densities that would lead to the *Chandra* count rate upper limits. Finally, we assumed  $\Gamma = 1$  and  $N_{\text{H}} = 5 \times 10^{22} \text{ cm}^{-2}$  and calculated the *Chandra* count rates that would be predicted for the *INTEGRAL* fluxes. In Table 4, we report the upper limits on  $\Gamma$  (first calculation),  $N_{\text{H}}$  (second calculation), and the variability factor, which is the ratio of the predicted count rate to the upper limit on the count rate.

## 4. DISCUSSION

The result of the *Chandra* observations is that we have identified X-ray counterparts to IGR J14091–6108, IGR J18088–

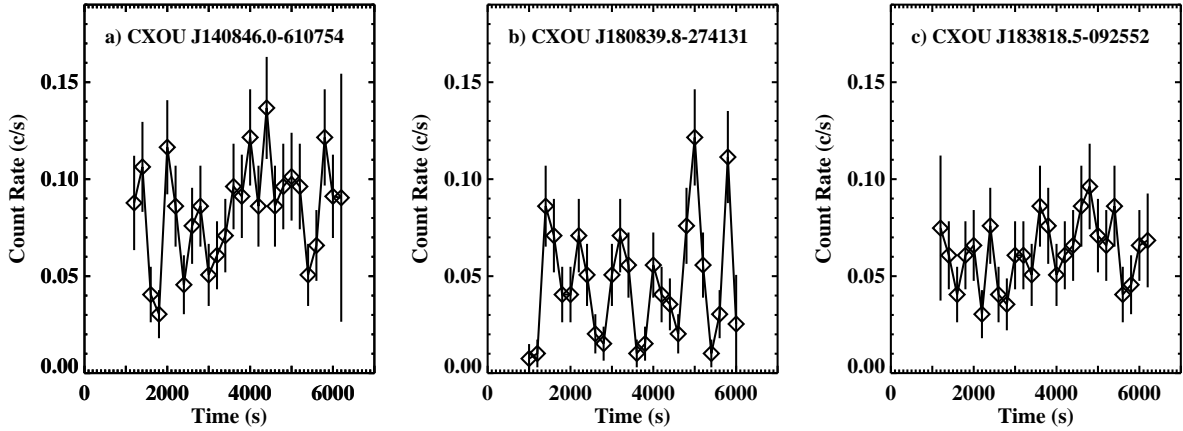


FIG. 3.— *Chandra* 0.3–10 keV light curves with 200 s time bins for (a) CXOU J140846.0–610754, (b) CXOU J180839.8–274131, and (c) CXOU J183818.5–092552.

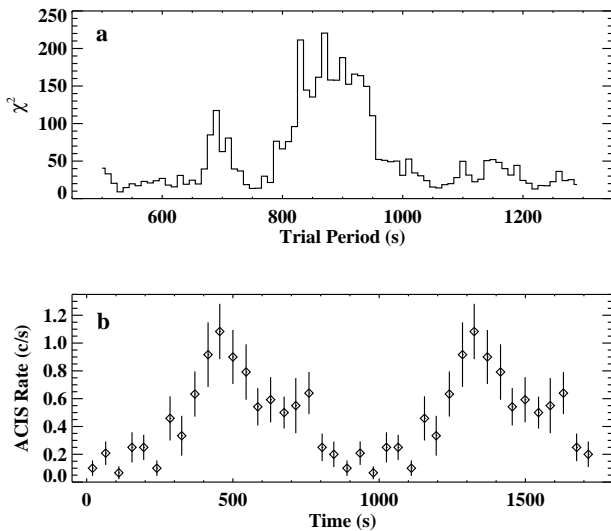


FIG. 4.— Results of folding the *Chandra* light curve for CXOU J180839.8–274131. (a) The resulting  $\chi^2$  value when fitting the light curve with a constant after folding on trial periods between 500 s and 1300 s. (b) The folded light curve for a period of 870 s, which is the trial period that gave the maximum  $\chi^2$ .

2741, and IGR J18381–0924, and henceforth, we will use the IGR names to refer to these *Chandra*/*INTEGRAL* sources. For IGR J14091–6108 and IGR J18088–2741, the *Chandra* positions provide unique near-IR identifications, and for IGR J18381–0924, there are two near-IR sources compatible with the *Chandra* position. Here, we discuss the nature of the three sources and then the implications of the parameter limits on the other five sources.

#### 4.1. IGR J14091–6108

There is clear evidence that IGR J14091–6108 is in our Galaxy. The iron line detected in its spectrum is not redshifted, and the low measured column density indicates that it is relatively nearby: the Galactic column density along this line of sight ( $l = 312.13^\circ$ ,  $b = +0.35^\circ$ ) is  $5.4 \times 10^{22} \text{ cm}^{-2}$ , but we measure an upper limit of  $< 1.7 \times 10^{22} \text{ cm}^{-2}$ . Although we do not know its intrinsic near-IR spectral shape, the fact that the VISTA magnitudes do not indicate strong reddening

is also consistent with a relatively small distance, probably less than a few kpc.

The hard X-ray spectrum ( $\Gamma = 0.6 \pm 0.4$ ) favors the possibilities that either the compact object is a magnetic white dwarf in a CV (Revnivtsev et al. 2008) or that it is an accreting neutron star with a high,  $\sim 10^{12}$  G, magnetic field (Coburn et al. 2002). Nearly all of the accreting black holes that we know of have photon indices softer than  $\Gamma \approx 1.2$ – $1.4$ , even in their hard state (McClintock & Remillard 2006), and neutron stars with weaker magnetic fields have even softer spectra. An isolated neutron star, such as a magnetar, could have a hard spectrum, but the brightness of IGR J14091–6108 in the near-IR requires a stellar companion. A CV with a spectrum as hard as we observe would almost certainly belong to the class of Intermediate Polars (IPs, Scaringi et al. 2010), where the white dwarf magnetic field is strong enough to truncate the accretion disk and funnel material onto the magnetic poles. In the neutron star case, nearly all high magnetic field neutron stars in binary systems are found in HMXBs. Thus, it is likely that IGR J14091–6108 is either a CV/IP or a neutron star HMXB.

The source’s X-ray luminosity could provide a way to distinguish between the different hypotheses because CV/IPs are not known to exceed values of  $\sim 10^{35} \text{ erg s}^{-1}$ . With the 0.3–10 keV unabsorbed flux being  $(2.2^{+0.4}_{-0.3}) \times 10^{-12} \text{ erg cm}^{-2} \text{ s}^{-1}$ , the luminosity is  $3 \times 10^{32} d_1^2 \text{ erg s}^{-1}$ , where  $d_1$  is the distance in kpc, which leaves both possibilities open since neutron star HMXBs can have low luminosities. The CV hypothesis is somewhat favored by the fact that neutron star HMXBs typically have iron line equivalent widths of 200 eV or less (Giménez-García et al. 2015) while we measure  $EW = 1.2^{+0.9}_{-0.7} \text{ keV}$ . Although there are some HMXBs with unusually high iron line strengths (Barragán et al. 2009; Giménez-García et al. 2015), these only occur in cases where the continuum is absorbed by material intrinsic to the system (e.g., a stellar wind), but the low  $N_{\text{H}}$  for IGR J14091–6108 makes this possibility unlikely. While an  $EW$  of 1.2 keV is also somewhat high for a CV, values in excess of 400 eV (combining all iron ionization states) are not unusual (Hellier & Mukai 2004). An even higher equivalent width for the iron lines was reported for a combined spectrum consisting of *Chandra* sources in the Galactic Center region (Muno et al. 2004), and those spectra also show evidence for emission lines from argon and calcium in the 3–

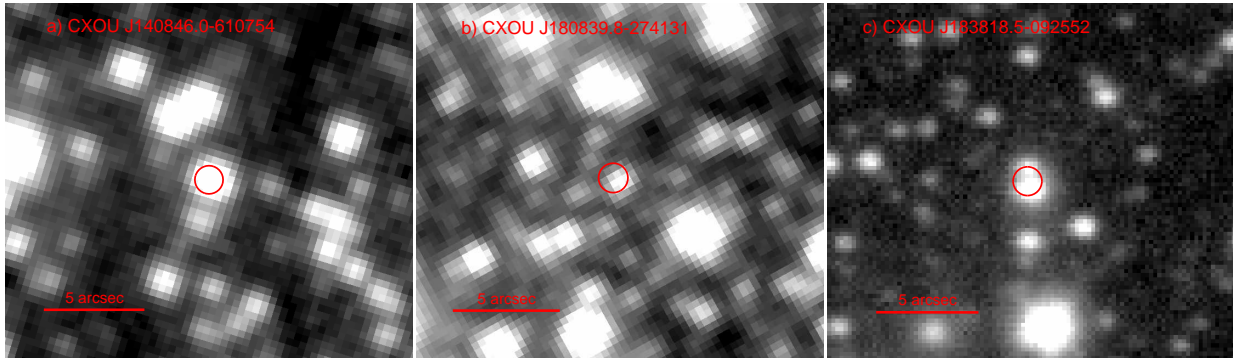


FIG. 5.— (a)  $K_s$ -band image of CXOU J140846.0–610754 from VISTA/VVV, (b)  $K_s$ -band image of CXOU J180839.8–274131 from VISTA/VVV, and (c)  $K$ -band image of CXOU J183818.5–092552 from UKIDSS. The *Chandra* error circle is shown.

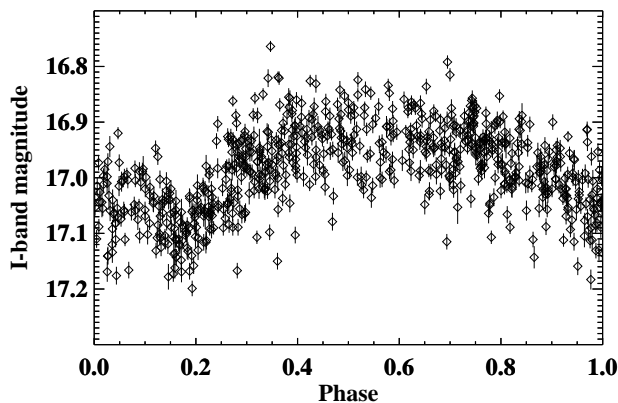


FIG. 6.— OGLE  $I$ -band light curve for VVV J180839.77–274131.7 after folding on the 0.28494563 day period listed in the OGLE-III Catalog of Variable Stars (Soszyński et al. 2011).

4 keV range. As discussed in section 3.2, the IGR J14091–6108 spectrum shows positive residuals at 4 keV, but they are not statistically significant. Munro et al. (2004) interpret the Galactic Center point source spectrum as being due to a thermal plasma model, and they suggest that the emission is from a population of CV/IPs.

#### 4.2. IGR J18088–2741

A key piece of evidence that sheds light on the nature of IGR J18088–2741 is its identification with OGLE-BLG-RRLYR-14363, which has a 6.84 hr optical period. Although it is contained in a catalog of RR Lyrae stars (Soszyński et al. 2011), which produce periodic optical variations due to stellar pulsations, the fact that we detect this source with such a hard X-ray spectrum ( $\Gamma = -0.7^{+0.4}_{-0.3}$ ) eliminates the possibility that the emission is coming from an isolated star. The combination of the hard spectrum and the optical periodicity strongly suggests that we are seeing a binary system with a compact object, but the origin of the periodicity and the type of compact object are uncertain. In many accreting systems, an optical modulation is seen at the orbital period of the system due to the heating of one side of the optical companion. However, such light curves are often approximately sinusoidal, and the fact that the IGR J18088–2741 optical light curve is more complex (see Figure 6) may indicate that we are also seeing light from the accretion disk. We also considered the possibility that we are seeing the superhump period, which is related to tidal stresses in the accretion disks of CVs, but these are

much more common for CVs with orbital periods less than a few hours (Patterson et al. 2005).

Similarly to IGR J14091–6108, the very hard X-ray spectrum of IGR J18088–2741 favors the possibilities that either the source is a CV/IP or that it is a highly magnetized neutron star in an X-ray binary. Although the 800–950 s X-ray period needs to be confirmed with a longer observation, by itself, such a period does not immediately distinguish between the CV/IP and X-ray binary possibilities. However, the X-ray binary hypothesis is challenged by the fact that such slow rotators are only common in HMXBs, while, if the 6.84 hr period is orbital, then this would be extremely short for an HMXB, where periods of days to weeks, or even months, are typical.

Given that its 0.3–10 keV unabsorbed flux is  $3 \times 10^{-12} \text{ erg cm}^{-2} \text{ s}^{-1}$ , this source would need to lie at a distance in excess of 15 kpc for its luminosity to challenge the CV/IP limit of  $\sim 10^{35} \text{ erg s}^{-1}$ . As the Galactic column density is  $3 \times 10^{21} \text{ cm}^{-2}$  along this line of sight ( $l = 3.65^\circ$ ,  $b = -3.84^\circ$ ), the X-ray measured  $N_{\text{H}}$  (see Table 2) does not provide any indication of the distance. However, the fact that the optical extinction is low (see Table 3) favors a much smaller distance than 15 kpc, and with the luminosity being  $4 \times 10^{32} d_1^2 \text{ erg s}^{-1}$ , it is clear that this constraint does not rule out either possibility.

#### 4.3. IGR J18381–0924

The X-ray spectrum of IGR J18381–0924 is significantly different from the other two sources. The power-law is consistent with being softer,  $\Gamma = 1.5^{+0.5}_{-0.4}$  (for the *Chandra*-only fit), and there is no evidence for a cutoff up to 86 keV. Also, the spectrum is absorbed, and the measured  $N_{\text{H}} = (4 \pm 1) \times 10^{22} \text{ cm}^{-2}$  is marginally higher than the Galactic column density along this line of sight ( $l = 23.05^\circ$ ,  $b = -1.36^\circ$ ) of  $2.1 \times 10^{22} \text{ cm}^{-2}$ . Based on just the X-ray spectrum, the source could be Galactic or extragalactic: if it is Galactic, then an accreting black hole in the hard state is a possibility; and, if it is extragalactic, then its properties are consistent with those of AGN. Both types of sources might have radio counterparts, but there is no radio counterpart listed in the NRAO VLA Sky Survey (NVSS, Condon et al. 1998) even though this area of the sky was covered. The interpretation of this source as being Galactic starts to become problematic when one considers the lack of X-ray variability on long and short time scales since most Galactic black holes are X-ray transients. Even stronger evidence in favor of an extragalactic nature comes from the fact that the two possible near-IR counterparts are identified as galaxies. Thus, we conclude that IGR J18381–0924 is proba-

bly an AGN.

#### 4.4. Implications of the Upper Limits for the Other Five Fields

For the sources without clear *Chandra* counterparts (IGR J15335–5420, IGR J17164–3803, IGR J17174–2436, IGR J17306–2015, and IGR J20107+4534), Table 4 shows that the sources need to be extremely hard or highly variable in order to explain the *Chandra* upper limits. Values of  $\Gamma = -1.2$  to  $-1.5$  may be possible for some types of Galactic sources (e.g., IGR J18088–2741), but  $\Gamma = -2.9$  is too hard to be realistic. Explaining the low *Chandra* count rates by high column densities requires value of  $N_{\text{H}}$  of  $\sim 2 \times 10^{24} \text{ cm}^{-2}$ . Such values occur very rarely in Galactic sources but have been seen for the most extreme obscured HMXB (Matt & Guainazzi 2003; Barragán et al. 2009). Such column densities occur relatively often for Seyfert 2 AGN (Brightman et al. 2015, and references therein), and we consider this a possibility for the nature of some of these sources. On the other hand, the low *Chandra* count rates can be explained by source variability with factors of  $> 11$ –60. Such variability is possible for many types of Galactic sources. The observations are consistent with either long-term (years to decades) or short-term (hours) variability.

#### 5. CONCLUSIONS AND FUTURE WORK

We conclude that IGR J14091–6108 and IGR J18088–2741 may be either CVs or HMXBs but that a CV is favored for the former source by the strong iron line, and a CV is strongly favored in the latter source if the 6.84 hr optical periodicity is the orbital period of the system. If the CV nature is confirmed by optical or near-IR spectroscopy, then these sources would join a group of 26 IGR CVs. An AGN nature is most likely for IGR J18381–0924. Follow-up optical or IR spectroscopy of the two candidate near-IR counterparts, which are both identified as galaxies in the UGPS catalog, is required to confirm that one or both of the counterparts are AGN. For the other

five IGR sources, the fact that we were not able to definitively determine a unique counterpart using the *Chandra* observations may indicate that these IGR sources are transient, highly variable, or that their spectra are extremely hard (either due to absorption or intrinsic spectral shape). Further observations of the sources listed in the Appendix may still provide a determination of the correct counterpart and the nature of these sources.

JAT and QW acknowledge partial support from the National Aeronautics and Space Administration (NASA) through *Chandra* Award Number GO4-15044X issued by the *Chandra* X-ray Observatory Center, which is operated by the Smithsonian Astrophysical Observatory under NASA contract NAS8-03060. RK acknowledges support from Russian Science Foundation (grant 14-22-00271). This work included observations with *INTEGRAL*, an ESA project with instruments and the science data center funded by ESA member states (especially the PI countries: Denmark, France, Germany, Italy, Switzerland, Spain), and Poland, and with the participation of Russia and the USA. This research has made use of the IGR Sources page maintained by J. Rodriguez and A. Bodaghee (<http://irfu.cea.fr/Sap/IGR-Sources>), the Vizier catalog access tool and the SIMBAD database, which are both operated at CDS, Strasbourg, France. This work is based in part on data obtained as part of the UKIRT Infrared Deep Sky Survey and also on data products from the VVV Survey observations made with the VISTA telescope at the ESO Paranal Observatory under program ID 179.B-2002. This publication makes use of data products from the Two Micron All Sky Survey, which is a joint project of the University of Massachusetts and the Infrared Processing and Analysis Center/California Institute of Technology, funded by NASA and the National Science Foundation. We acknowledge suggestions from an anonymous referee, which led to improvements in the manuscript.

#### APPENDIX

Section 3.1 describes how we used *wavdetect* to find 115 *Chandra* sources in the eight ACIS-I fields. A full source lists is provided in Table 5, and here we provide a more thorough explanation of how the values in those tables were derived. The sources are listed in order of how far they lie from the centers of each of the *INTEGRAL* error circles, and this angle ( $\theta$ ), in arcminutes, is given in the tables.

To determine the source positions, we started with the values provided by *wavdetect*. In order to reduce the systematic uncertainties due to the absolute *Chandra* pointing, we looked for matches to the *Chandra* sources in near-IR catalogs. We used the VISTA Variables in the Via Lactea (VVV) near-IR catalog (Minniti et al. 2010) for sources in the IGR J14091–6108, IGR J15335–5420, IGR J17164–3803, and IGR J18088–2741 fields. Due to the incomplete sky coverage of the VVV catalog, counterparts for other fields were not found in VVV. Thus, for IGR J17174–2436 and IGR J18381–0924, we searched the UKIRT Infrared Deep Sky Survey (UKIDSS) catalog (Lawrence et al. 2007), and for IGR J17306–2015 and IGR J20107+4534, we searched the 2 Micron All Sky Survey (2MASS) catalog (Cutri et al. 2003). For each field, we compiled a list of potential near-IR counterparts, and ran *wcs\_match* to compare the *Chandra* and near-IR lists, determine likely matches, and calculate the astrometric correction. When we ran *wcs\_match*, we used the “residlim” parameter to only include sources for which the *Chandra* and near-IR positions agree to better than  $1''$  in order to discard unlikely matches as well as many of the *Chandra* sources with larger statistical position errors. We only found one match in the IGR J17174–2436, two matches in the IGR J17306–2015 field, and three matches in the IGR J18381–0924 field, which are not enough to calculate a reliable position shift. For the other five fields, we found between 5 and 15 matches, and the number of matches for each field is given in Table 6. Although *wcs\_match* can consider both linear translations and coordinate rotations to optimize source matches, we restricted the shifts to linear translations since there are three fields where we only have five matches. The shifts determined by *wcs\_match* are given in Table 6. We used *wcs\_update* to apply these shifts to the positions reported in Table 5.

The position uncertainties have statistical and systematic contributions. Since the *Chandra* PSF becomes significantly larger for off-axis angles, the statistical uncertainty depends on the number of counts detected for each source as well as its off-axis angle. We used Equation 5 from Hong et al. (2005) to calculate the statistical uncertainty. Although this equation gives a 95% confidence error circle radius ( $2\sigma$ ), we reduced the radius to 90% confidence ( $1.7\sigma$ ) by multiplying by a factor of  $1.7/2.0$ . For the systematic contribution, we assumed a 90% confidence error of  $0.''64$  (Weisskopf 2005). While this is an overestimate for the



fields where we shifted coordinates, we could not determine how much these shifts decrease the systematic position uncertainty due to the relatively small number of X-ray/near-IR matches. The total position uncertainty quoted in the tables is the value obtained by adding the statistical and systematic values in quadrature.

## REFERENCES

- Barragán, L., Wilms, J., Pottschmidt, K., et al. 2009, *A&A*, 508, 1275
- Bird, A. J., Bazzano, A., Bassani, L., et al. 2010, *ApJS*, 186, 1
- Bodaghee, A., Rahoui, F., Tomsick, J. A., & Rodriguez, J. 2012, *ApJ*, 751, 113
- Brightman, M., Baloković, M., Stern, D., et al. 2015, *ApJ*, 805, 41
- Caballero, I., Zurita Heras, J. A., Mattana, F., et al. 2013, arXiv:1304.1349
- Cash, W., 1979, *ApJ*, 228, 939
- Churazov, E., Sunyaev, R., Isern, J., et al. 2014, *Nature*, 512, 406
- Churazov, E., Sunyaev, R., Sazonov, S., Revnivtsev, M., & Varshalovich, D. 2005, *MNRAS*, 357, 1377
- Coburn, W., Heindl, W. A., Rothschild, R. E., et al. 2002, *ApJ*, 580, 394
- Condon, J. J., Cotton, W. D., Greisen, E. W., et al. 1998, *AJ*, 115, 1693
- Cutri, R. M., Skrutskie, M. F., van Dyk, S., et al. 2003, 2MASS All Sky Catalog of Point Sources (NASA/IPAC Infrared Science Archive)
- Dame, T. M., Hartmann, D., & Thaddeus, P. 2001, *ApJ*, 547, 792
- Filliatre, P., & Chaty, S. 2004, *ApJ*, 616, 469
- Fiocchi, M., Bassani, L., Bazzano, A., et al. 2010, *ApJ*, 720, 987
- Freeman, P. E., Kashyap, V., Rosner, R., & Lamb, D. Q. 2002, *ApJS*, 138, 185
- Garmire, G. P., Bautz, M. W., Ford, P. G., Nousek, J. A., & Ricker, G. R. 2003, *Proc. SPIE*, 4851, 28
- Gehrels, N., 1986, *ApJ*, 303, 336
- Giménez-García, A., Torrejón, J. M., Eikmann, W., et al. 2015, *A&A*, 576, A108
- Hellier, C., & Mukai, K. 2004, *MNRAS*, 352, 1037
- Hong, J., van den Berg, M., Schlegel, E. M., et al. 2005, *ApJ*, 635, 907
- Kalberla, P. M. W., Burton, W. B., Hartmann, D., et al. 2005, *A&A*, 440, 775
- Karasev, D. I., Lutovinov, A. A., Revnivtsev, M. G., & Krivonos, R. A. 2012, *Astronomy Letters*, 38, 629
- Krivonos, R., Revnivtsev, M., Tsygankov, S., et al. 2010, *A&A*, 519, A107
- Krivonos, R., Tsygankov, S., Lutovinov, A., et al. 2012, *A&A*, 545, A27
- Landi, R., Bassani, L., Masetti, N., et al. 2012, *The Astronomer's Telegram*, 4165
- Lawrence, A., Warren, S. J., Almaini, O., et al. 2007, *MNRAS*, 379, 1599
- Matt, G., & Guainazzi, M. 2003, *MNRAS*, 341, L13
- McClintock, J. E., & Remillard, R. A. 2006, *Black hole binaries, Compact Stellar X-ray Sources*, ed. W. Lewin & M. van der Klis (Cambridge: Cambridge Univ. Press), 157
- Minniti, D., Lucas, P. W., Emerson, J. P., et al. 2010, *New Astronomy*, 15, 433
- Muno, M. P., Arabadjis, J. S., Baganoff, F. K., et al. 2004, *ApJ*, 613, 1179
- Neguera, I., Smith, D. M., Reig, P., Chaty, S., & Torrejón, J. M. 2006, in *The X-ray Universe 2005*, ed. A. Wilson (ESA SP-604; Noordwijk: ESA), 165
- Nowak, M. A., Paizis, A., Rodriguez, J., et al. 2012, *ApJ*, 757, 143
- Paizis, A., Nowak, M. A., Rodriguez, J., et al. 2012, *ApJ*, 755, 52
- Paizis, A., Nowak, M. A., Wilms, J., et al. 2011, *ApJ*, 738, 183
- Papitto, A., Ferrigno, C., Bozzo, E., et al. 2013, *Nature*, 501, 517
- Patterson, J., Kemp, J., Harvey, D. A., et al. 2005, *PASP*, 117, 1204
- Pavan, L., Bozzo, E., Pühlhofer, G., et al. 2011, *A&A*, 533, A74
- Pellizza, L. J., Chaty, S., & Negueruela, I. 2006, *A&A*, 455, 653
- Ratti, E. M., Bassa, C. G., Torres, M. A. P., et al. 2010, *MNRAS*, 408, 1866
- Revnivtsev, M., Sazonov, S., Krivonos, R., Ritter, H., & Sunyaev, R. 2008, *A&A*, 489, 1121
- Romano, P., Krimm, H. A., Palmer, D. M., et al. 2014, *A&A*, 562, A2
- Scaringi, S., Bird, A. J., Norton, A. J., et al. 2010, *MNRAS*, 401, 2207
- Sidoli, L., Esposito, P., Sguera, V., et al. 2013, *MNRAS*, 429, 2763
- Smith, D. M., Heindl, W. A., Markwardt, C. B., et al. 2006, *ApJ*, 638, 974
- Soszyński, I., Dziembowski, W. A., Udalski, A., et al. 2011, *Acta Astron.*, 61, 1
- Tomsick, J. A., Bodaghee, A., Chaty, S., et al. 2012a, *ApJ*, 754, 145
- Tomsick, J. A., Bodaghee, A., Rodriguez, J., et al. 2012b, *ApJ*, 750, L39
- Tomsick, J. A., Chaty, S., Rodriguez, J., et al. 2006, *ApJ*, 647, 1309
- Tomsick, J. A., Chaty, S., Rodriguez, J., Walter, R., & Kaaret, P. 2009, *ApJ*, 701, 811
- Tomsick, J. A., Kalemci, E., Kaaret, P., et al. 2008, *ApJ*, 680, 593
- Tomsick, J. A., Krivonos, R., Rahoui, F., et al. 2015, *MNRAS*, 449, 597
- Tomsick, J. A., Rahoui, F., Krivonos, R., et al. 2014, *The Astronomer's Telegram*, 6793
- Ubertini, P., Lebrun, F., Di Cocco, G., et al. 2003, *A&A*, 411, L131
- Verner, D. A., Ferland, G. J., Korista, K. T., & Yakovlev, D. G. 1996, *ApJ*, 465, 487
- Walter, R., Lutovinov, A. A., Bozzo, E., & Tsygankov, S. S. 2015, *A&A Review*, 23, 2
- Walter, R., Zurita Heras, J., Bassani, L., et al. 2006, *A&A*, 453, 133
- Weisskopf, M. C., 2005, arXiv:astro-ph/0503091
- Wilms, J., Allen, A., & McCray, R. 2000, *ApJ*, 542, 914
- Winkler, C., Courvoisier, T. J.-L., Di Cocco, G., et al. 2003, *A&A*, 411, L1

TABLE 1  
*Chandra* OBSERVATIONS

IGR Name	ObsID	$l^a$	$b^b$	Start Time	Exposure Time (s)	$N_{\text{sources}}^c$
J14091–6108	15789	312.13	+0.35	2013 Dec 7, 23.7 h UT	4912	18
J15335–5420	15790	325.18	+1.36	2014 Jun 4, 8.9 h UT	4912	8
J17164–3803	15788	349.07	+0.07	2014 Apr 15, 18.6 h UT	4912	12
J17174–2436	15797	0.19	+7.65	2014 Feb 27, 5.3 h UT	4902	14
J17306–2015	15796	5.52	+7.53	2015 Feb 8, 11.2 h UT	4906	7
J18088–2741	15794	3.65	–3.84	2014 Feb 16, 16.7 h UT	4915	29
J18381–0924	15791	23.05	–1.36	2014 Feb 15, 18.6 h UT	4912	14
J20107+4534	15795	81.39	+6.59	2013 Dec 21, 5.4 h UT	4912	13

<sup>a</sup>Galactic longitude measured by *INTEGRAL* (degrees)

<sup>b</sup>Galactic latitude measured by *INTEGRAL* (degrees)

<sup>c</sup>Number of *Chandra* sources detected in each field.

TABLE 2  
 SPECTRAL PARAMETERS

Parameter <sup>a</sup>	Units	<i>Chandra</i> -only	<i>Chandra</i> + <i>INTEGRAL</i>	
CXOU J140846.0–610754				
$N_{\text{H}}^b$	$10^{22} \text{ cm}^{-2}$	$1.0^{+0.7}_{-0.6}$	$0.8^{+0.7}_{-0.5}$	$0.6^{+0.6}_{-0.5}$
$\Gamma$	–	$0.6 \pm 0.4$	$0.3 \pm 0.5$	$0.1^{+0.4}_{-0.5}$
Unabsorbed Flux (0.3–10 keV)	$10^{-12} \text{ erg cm}^{-2} \text{ s}^{-1}$	$2.2^{+0.4}_{-0.3}$	$2.3 \pm 0.3$	$2.4 \pm 0.3$
$E_{\text{line}}$	keV	$6.6 \pm 0.2$	$6.6^{+0.4}_{-0.2}$	$6.6^{+0.3}_{-0.2}$
$\sigma_{\text{line}}$	keV	$0.2^{+0.4}_{-0.2}$	<0.6	<0.6
$N_{\text{line}}$	$10^{-5} \text{ ph cm}^{-2} \text{ s}^{-1}$	$3.0^{+2.3}_{-1.8}$	$3.4^{+3.6}_{-2.0}$	$3.0^{+1.9}_{-1.8}$
$E_{\text{fold}}$	keV	–	$13^{+10}_{-5}$	$14^{+11}_{-5}$
$N_{\text{INTEGRAL}}/N_{\text{Chandra}}^c$	–	–	$1.8^{+2.8}_{-1.1}$	$1.0^d$
$\chi^2/\text{dof}$	–	18.9/19	18.5/21	19.7/22
CXOU J180839.8–274131				
$N_{\text{H}}^b$	$10^{22} \text{ cm}^{-2}$	$0.2^{+1.0}_{-0.2}$	<0.7	<0.7
$\Gamma$	–	$-0.7^{+0.4}_{-0.3}$	$-1.5 \pm 0.4$	$-1.5^{+0.4}_{-0.2}$
Unabsorbed Flux (0.3–10 keV)	$10^{-12} \text{ erg cm}^{-2} \text{ s}^{-1}$	$3.5^{+0.7}_{-0.6}$	$2.8 \pm 0.5$	$2.8 \pm 0.4$
$E_{\text{fold}}$	keV	–	$5.1^{+1.6}_{-1.3}$	$4.8^{+1.1}_{-0.8}$
$N_{\text{INTEGRAL}}/N_{\text{Chandra}}^c$	–	–	$0.8^{+0.6}_{-0.4}$	$1.0^d$
$\chi^2/\text{dof}$	–	13.6/15	12.0/17	12.3/18
CXOU J183818.5–092552				
$N_{\text{H}}^b$	$10^{22} \text{ cm}^{-2}$	$4.0^{+1.3}_{-1.2}$	$4.3^{+1.4}_{-1.1}$	$3.8^{+0.9}_{-0.7}$
$\Gamma$	–	$1.5^{+0.5}_{-0.4}$	$1.6 \pm 0.4$	$1.4 \pm 0.1$
Unabsorbed Flux (0.3–10 keV)	$10^{-12} \text{ erg cm}^{-2} \text{ s}^{-1}$	$3.4^{+1.4}_{-0.6}$	$3.5^{+1.4}_{-0.7}$	$3.2 \pm 0.5$
$N_{\text{INTEGRAL}}/N_{\text{Chandra}}^c$	–	–	$1.6^{+2.1}_{-0.9}$	$1.0^d$
$\chi^2/\text{dof}$	–	14.4/22	20.4/25	21.2/26

<sup>a</sup>The errors on the parameters are 90% confidence.

<sup>b</sup>The column density is calculated assuming Wilms et al. (2000) abundances and Verner et al. (1996) cross sections. The Galactic column density (atomic and molecular Hydrogen) at the locations of CXOU J140846.0–610754, CXOU J180839.8–274131, and CXOU J183818.5–092552 are  $5.4 \times 10^{22} \text{ cm}^{-2}$ ,  $3.0 \times 10^{21} \text{ cm}^{-2}$ , and  $2.1 \times 10^{22} \text{ cm}^{-2}$ , respectively (Kalberla et al. 2005; Dame et al. 2001).

<sup>c</sup>The *INTEGRAL* normalization relative to *Chandra*.

<sup>d</sup>Fixed.

TABLE 3  
IR IDENTIFICATIONS

IR Source	Separation <sup>a</sup>	Magnitudes
CXOU J140846.0–610754		
VVV J140845.99–610754.1	0.''16	$Z = 16.165 \pm 0.005$
"	"	$Y = 15.806 \pm 0.005$
"	"	$J = 15.220 \pm 0.005$
"	"	$H = 14.833 \pm 0.007$
"	"	$K_s = 14.394 \pm 0.010$
CXOU J180839.8–274131		
VVV J180839.77–274131.7	0.''41	$Z = 16.77 \pm 0.06$
"	"	$Y = 16.65 \pm 0.07$
"	"	$J = 16.09 \pm 0.06$
"	"	$H = 15.82 \pm 0.08$
"	"	$K_s = 15.67 \pm 0.09$
CXOU J183818.5–092552		
UGPS J183818.59–092551.8	0.''47	$K \approx 14^b$
UGPS J183818.58–092552.9	0.''73	$K \approx 13$

<sup>a</sup>The angular separation between the *Chandra* position and the catalog position.

<sup>b</sup>As described in the text, the magnitudes listed in the UKIDSS catalog are not consistent with the images. Here, we provide estimates for the *K*-band magnitudes based on visual comparisons to other nearby sources.

TABLE 4  
LIMITS ON PARAMETERS FOR THE IGR SOURCES WITHOUT CLEAR COUNTERPARTS

IGR Name	Limit on ACIS Rate (c/s)	<i>INTEGRAL</i> Flux <sup>a</sup>	Limit on $\Gamma$	Limit on $N_H$ (cm <sup>-2</sup> )	Limit on Variability <sup>b</sup>
J15335–5420	<0.0034	$5.5 \times 10^{-12}$	<-1.5	$>1.80 \times 10^{24}$	>16
J17164–3803	<0.0057	$8.7 \times 10^{-12}$	<-1.5	$>1.75 \times 10^{24}$	>15
J17174–2436	<0.0063	$6.4 \times 10^{-12}$	<-1.2	$>1.50 \times 10^{24}$	>10
J17306–2015	<0.0025	$1.6 \times 10^{-11}$	<-2.9	$>2.85 \times 10^{24}$	>60
J20107+4534	<0.0062	$6.8 \times 10^{-12}$	<-1.2	$>1.55 \times 10^{24}$	>11

<sup>a</sup>The 17–60 keV flux in units of erg cm<sup>-2</sup> s<sup>-1</sup> from Krivonos et al. (2012).

<sup>b</sup>The ratio of the *Chandra* count rate assuming the *INTEGRAL* flux,  $\Gamma = 1$ , and  $N_H = 5 \times 10^{22}$  cm<sup>-2</sup> to the measured upper limit on the count rate.

TABLE 5 *Chandra* Sources in IGR Source Fields

Source Number	$\theta^a$ (arcminutes)	<i>Chandra</i> R.A. (J2000)	<i>Chandra</i> Decl. (J2000)	Position Uncertainty <sup>b</sup>	ACIS Counts <sup>c</sup>	Hardness <sup>d</sup>
IGR J14091-6108						
1	0.45	14 <sup>h</sup> 08 <sup>m</sup> 46 <sup>s</sup> .02	-61°07'54.''2	0.''69	405 <sup>+21</sup> <sub>-20</sub>	0.56 ± 0.06
2	1.13	14 <sup>h</sup> 08 <sup>m</sup> 36 <sup>s</sup> .70	-61°06'48.''1	0.''86	3.8 <sup>+3.2</sup> <sub>-2.2</sub>	< 0.53
3	1.18	14 <sup>h</sup> 08 <sup>m</sup> 42 <sup>s</sup> .96	-61°08'47.''7	0.''80	5.8 <sup>+3.6</sup> <sub>-2.4</sub>	< -0.09
4	1.58	14 <sup>h</sup> 08 <sup>m</sup> 31 <sup>s</sup> .37	-61°06'56.''1	0.''72	43 <sup>+18</sup> <sub>-7</sub>	> 0.70
5	1.59	14 <sup>h</sup> 08 <sup>m</sup> 30 <sup>s</sup> .19	-61°07'52.''2	0.''90	3.8 <sup>+3.2</sup> <sub>-1.9</sub>	> -0.27
6	2.08	14 <sup>h</sup> 08 <sup>m</sup> 27 <sup>s</sup> .89	-61°08'33.''5	0.''91	4.8 <sup>+3.4</sup> <sub>-2.2</sub>	< 0.04
7	2.50	14 <sup>h</sup> 08 <sup>m</sup> 49 <sup>s</sup> .80	-61°05'14.''2	0.''76	23 <sup>+6</sup> <sub>-4</sub>	-0.05 ± 0.28
8	2.66	14 <sup>h</sup> 08 <sup>m</sup> 34 <sup>s</sup> .99	-61°05'08.''6	0.''78	18 <sup>+3</sup> <sub>-4</sub>	< -0.40
9	3.87	14 <sup>h</sup> 08 <sup>m</sup> 52 <sup>s</sup> .79	-61°11'18.''4	1.''41	4.5 <sup>+3.4</sup> <sub>-2.2</sub>	< 0.06
10	4.35	14 <sup>h</sup> 08 <sup>m</sup> 40 <sup>s</sup> .33	-61°03'16.''8	1.''40	6.0 <sup>+3.8</sup> <sub>-2.8</sub>	0.07 ± 0.72
11	5.10	14 <sup>h</sup> 08 <sup>m</sup> 32 <sup>s</sup> .36	-61°12'32.''2	1.''65	6.8 <sup>+4.0</sup> <sub>-2.8</sub>	< -0.11
12	7.28	14 <sup>h</sup> 08 <sup>m</sup> 16 <sup>s</sup> .64	-61°01'04.''6	3.''04	8.0 <sup>+4.6</sup> <sub>-3.4</sub>	< -0.46
13	7.64	14 <sup>h</sup> 09 <sup>m</sup> 42 <sup>s</sup> .67	-61°10'15.''2	2.''60	11 <sup>+4</sup> <sub>-3</sub>	< -0.16
14	7.83	14 <sup>h</sup> 09 <sup>m</sup> 44 <sup>s</sup> .69	-61°05'08.''7	2.''08	17 <sup>+6</sup> <sub>-5</sub>	> 0.22
15	8.32	14 <sup>h</sup> 08 <sup>m</sup> 13 <sup>s</sup> .99	-61°15'09.''3	7.''18	4.6 <sup>+4.6</sup> <sub>-3.5</sub>	—
16	8.66	14 <sup>h</sup> 09 <sup>m</sup> 04 <sup>s</sup> .29	-61°15'53.''8	1.''23	75 <sup>+10</sup> <sub>-9</sub>	> 0.77
17	8.80	14 <sup>h</sup> 08 <sup>m</sup> 18 <sup>s</sup> .16	-61°15'52.''5	2.''20	23 <sup>+7</sup> <sub>-6</sub>	> 0.56
18	9.28	14 <sup>h</sup> 09 <sup>m</sup> 59 <sup>s</sup> .91	-61°08'13.''7	1.''94	34 <sup>+8</sup> <sub>-7</sub>	0.13 ± 0.24
IGR J15335-5420						
1	0.65	15 <sup>h</sup> 33 <sup>m</sup> 34 <sup>s</sup> .98	-54°21'03.''2	0.''80	4.9 <sup>+3.4</sup> <sub>-2.2</sub>	< 0.03
2	1.48	15 <sup>h</sup> 33 <sup>m</sup> 34 <sup>s</sup> .87	-54°23'03.''9	0.''85	4.8 <sup>+3.4</sup> <sub>-2.2</sub>	> -0.05
3	3.22	15 <sup>h</sup> 33 <sup>m</sup> 30 <sup>s</sup> .98	-54°18'24.''5	1.''15	4.7 <sup>+3.4</sup> <sub>-2.2</sub>	< 0.30
4	4.31	15 <sup>h</sup> 33 <sup>m</sup> 39 <sup>s</sup> .34	-54°17'24.''8	1.''35	6.2 <sup>+3.8</sup> <sub>-2.6</sub>	> 0.13
5	5.12	15 <sup>h</sup> 32 <sup>m</sup> 57 <sup>s</sup> .89	-54°22'14.''6	1.''29	11 <sup>+5</sup> <sub>-3</sub>	> 0.14
6	5.25	15 <sup>h</sup> 33 <sup>m</sup> 04 <sup>s</sup> .40	-54°18'23.''1	2.''22	4.7 <sup>+3.6</sup> <sub>-2.4</sub>	< 0.42
7	8.19	15 <sup>h</sup> 32 <sup>m</sup> 47 <sup>s</sup> .81	-54°26'32.''7	2.''31	17 <sup>+6</sup> <sub>-5</sub>	0.09 ± 0.38
8	8.38	15 <sup>h</sup> 33 <sup>m</sup> 21 <sup>s</sup> .52	-54°29'50.''1	4.''42	7.9 <sup>+4.9</sup> <sub>-3.7</sub>	< 0.17
IGR J17164-3803						
1	0.17	17 <sup>h</sup> 16 <sup>m</sup> 29 <sup>s</sup> .26	-38°02'04.''9	0.''75	7.9 <sup>+4.0</sup> <sub>-2.8</sub>	< 0.11
2	1.87	17 <sup>h</sup> 16 <sup>m</sup> 26 <sup>s</sup> .97	-38°00'07.''8	0.''73	28 <sup>+6</sup> <sub>-5</sub>	0.36 ± 0.26
3	2.26	17 <sup>h</sup> 16 <sup>m</sup> 33 <sup>s</sup> .23	-37°59'46.''9	0.''93	4.8 <sup>+3.4</sup> <sub>-2.2</sub>	< 0.30
4	2.89	17 <sup>h</sup> 16 <sup>m</sup> 19 <sup>s</sup> .94	-38°04'06.''1	1.''35	2.8 <sup>+2.9</sup> <sub>-1.7</sub>	< 0.61
5	3.82	17 <sup>h</sup> 16 <sup>m</sup> 17 <sup>s</sup> .33	-37°58'58.''9	0.''94	12 <sup>+5</sup> <sub>-4</sub>	> 0.22
6	4.01	17 <sup>h</sup> 16 <sup>m</sup> 09 <sup>s</sup> .39	-38°02'22.''6	1.''23	6.4 <sup>+3.8</sup> <sub>-2.6</sub>	> -0.28
7	4.34	17 <sup>h</sup> 16 <sup>m</sup> 49 <sup>s</sup> .50	-38°03'48.''3	1.''67	4.4 <sup>+3.4</sup> <sub>-2.2</sub>	< 0.09
8	5.83	17 <sup>h</sup> 16 <sup>m</sup> 02 <sup>s</sup> .06	-38°04'02.''9	1.''37	14 <sup>+5</sup> <sub>-4</sub>	0.05 ± 0.40
9	6.57	17 <sup>h</sup> 17 <sup>m</sup> 00 <sup>s</sup> .25	-37°59'19.''0	2.''96	6.1 <sup>+4.1</sup> <sub>-3.0</sub>	< 0.04
10	6.87	17 <sup>h</sup> 16 <sup>m</sup> 02 <sup>s</sup> .99	-38°06'22.''2	1.''97	12 <sup>+5</sup> <sub>-4</sub>	0.17 ± 0.46
11	7.17	17 <sup>h</sup> 16 <sup>m</sup> 58 <sup>s</sup> .28	-37°57'30.''7	1.''54	21 <sup>+6</sup> <sub>-5</sub>	> 0.35
12	7.29	17 <sup>h</sup> 16 <sup>m</sup> 56 <sup>s</sup> .86	-38°06'52.''0	1.''52	23 <sup>+6</sup> <sub>-5</sub>	0.13 ± 0.29
IGR J17174-2436						
1	1.92	17 <sup>h</sup> 17 <sup>m</sup> 20 <sup>s</sup> .44	-24°33'58.''4	0.''83	6.8 <sup>+3.8</sup> <sub>-2.6</sub>	< 0.22
2	2.75	17 <sup>h</sup> 17 <sup>m</sup> 10 <sup>s</sup> .65	-24°34'06.''6	0.''89	7.7 <sup>+4.0</sup> <sub>-2.8</sub>	-0.02 ± 0.58
3	2.92	17 <sup>h</sup> 17 <sup>m</sup> 32 <sup>s</sup> .16	-24°35'03.''2	0.''76	29 <sup>+6</sup> <sub>-5</sub>	0.17 ± 0.24
4	2.96	17 <sup>h</sup> 17 <sup>m</sup> 07 <sup>s</sup> .74	-24°34'49.''3	1.''41	2.6 <sup>+2.9</sup> <sub>-1.7</sub>	< 0.67
5	2.97	17 <sup>h</sup> 17 <sup>m</sup> 12 <sup>s</sup> .49	-24°33'26.''6	1.''41	2.6 <sup>+2.9</sup> <sub>-1.7</sub>	< 0.67
6	4.18	17 <sup>h</sup> 17 <sup>m</sup> 23 <sup>s</sup> .94	-24°31'49.''3	1.''43	5.2 <sup>+3.6</sup> <sub>-2.4</sub>	< 0.13
7	4.95	17 <sup>h</sup> 16 <sup>m</sup> 58 <sup>s</sup> .26	-24°36'29.''2	0.''90	31 <sup>+6</sup> <sub>-5</sub>	0.11 ± 0.24
8	5.24	17 <sup>h</sup> 17 <sup>m</sup> 42 <sup>s</sup> .86	-24°36'12.''6	1.''34	11 <sup>+5</sup> <sub>-3</sub>	0.30 ± 0.49
9	5.41	17 <sup>h</sup> 17 <sup>m</sup> 39 <sup>s</sup> .59	-24°38'55.''5	2.''40	4.6 <sup>+3.6</sup> <sub>-2.4</sub>	> -0.12
10	6.95	17 <sup>h</sup> 17 <sup>m</sup> 24 <sup>s</sup> .06	-24°42'46.''8	2.''79	7.7 <sup>+4.0</sup> <sub>-2.8</sub>	> -0.07
11	7.01	17 <sup>h</sup> 17 <sup>m</sup> 40 <sup>s</sup> .13	-24°30'36.''2	2.''85	7.7 <sup>+4.0</sup> <sub>-2.8</sub>	-0.08 ± 0.66
12	7.05	17 <sup>h</sup> 17 <sup>m</sup> 02 <sup>s</sup> .98	-24°29'58.''7	1.''70	17 <sup>+6</sup> <sub>-5</sub>	0.14 ± 0.37
13	7.12	17 <sup>h</sup> 16 <sup>m</sup> 48 <sup>s</sup> .88	-24°34'51.''1	2.''49	10 <sup>+5</sup> <sub>-4</sub>	0.34 ± 0.58
14	7.99	17 <sup>h</sup> 17 <sup>m</sup> 13 <sup>s</sup> .11	-24°43'44.''3	4.''11	7.4 <sup>+4.7</sup> <sub>-3.6</sub>	< 0.41
IGR J17306-2015						
1	1.26	17 <sup>h</sup> 30 <sup>m</sup> 24 <sup>s</sup> .81	-20°17'03.''3	0.''75	12 <sup>+5</sup> <sub>-3</sub>	0.16 ± 0.43
2	1.45	17 <sup>h</sup> 30 <sup>m</sup> 20 <sup>s</sup> .40	-20°14'36.''3	0.''88	3.9 <sup>+3.2</sup> <sub>-1.9</sub>	> -0.25
3	2.91	17 <sup>h</sup> 30 <sup>m</sup> 30 <sup>s</sup> .27	-20°13'20.''0	0.''95	6.8 <sup>+3.8</sup> <sub>-2.6</sub>	-0.16 ± 0.65
4	3.04	17 <sup>h</sup> 30 <sup>m</sup> 33 <sup>s</sup> .99	-20°13'55.''8	1.''42	2.8 <sup>+2.9</sup> <sub>-1.7</sub>	—
5	6.66	17 <sup>h</sup> 29 <sup>m</sup> 58 <sup>s</sup> .31	-20°12'53.''0	2.''68	7.2 <sup>+4.3</sup> <sub>-3.1</sub>	< -0.13
6	6.76	17 <sup>h</sup> 30 <sup>m</sup> 20 <sup>s</sup> .66	-20°22'32.''2	2.''78	7.1 <sup>+4.3</sup> <sub>-3.1</sub>	< -0.44
7	7.96	17 <sup>h</sup> 30 <sup>m</sup> 50 <sup>s</sup> .39	-20°10'52.''1	2.''73	12 <sup>+5</sup> <sub>-4</sub>	-0.01 ± 0.47
IGR J18088-2741						
1	0.38	18 <sup>h</sup> 08 <sup>m</sup> 58 <sup>s</sup> .55	-27°41'48.''9	0.''76	6.9 <sup>+3.8</sup> <sub>-2.6</sub>	-0.15 ± 0.64
2	1.42	18 <sup>h</sup> 09 <sup>m</sup> 06 <sup>s</sup> .57	-27°42'00.''2	0.''88	3.8 <sup>+3.6</sup> <sub>-1.9</sub>	< 0.96
3	1.65	18 <sup>h</sup> 08 <sup>m</sup> 53 <sup>s</sup> .76	-27°42'34.''8	0.''86	4.8 <sup>+3.4</sup> <sub>-2.2</sub>	< 0.29

TABLE 5 Continued

Source Number	$\theta^a$ (arcminutes)	Chandra R.A. (J2000)	Chandra Decl. (J2000)	Position Uncertainty <sup>b</sup>	ACIS Counts <sup>c</sup>	Hardness <sup>d</sup>
4	1.68	18 <sup>h</sup> 09 <sup>m</sup> 03 <sup>s</sup> .59	-27° 40' 15.''6	0.''83	5.8 <sup>+3.6</sup> <sub>-2.4</sub>	> -0.41
5	2.21	18 <sup>h</sup> 08 <sup>m</sup> 50 <sup>s</sup> .40	-27° 41' 26.''1	0.''84	7.8 <sup>+4.0</sup> <sub>-2.8</sub>	< 0.11
6	2.21	18 <sup>h</sup> 08 <sup>m</sup> 58 <sup>s</sup> .14	-27° 39' 36.''6	0.''77	16 <sup>+3.4</sup> <sub>-4.4</sub>	-0.01 ± 0.36
7	2.27	18 <sup>h</sup> 09 <sup>m</sup> 07 <sup>s</sup> .57	-27° 43' 21.''5	0.''94	4.8 <sup>+3.4</sup> <sub>-2.4</sub>	< 0.30
8	2.29	18 <sup>h</sup> 08 <sup>m</sup> 58 <sup>s</sup> .24	-27° 44' 00.''9	0.''94	4.8 <sup>+3.4</sup> <sub>-2.4</sub>	< 0.30
9	2.61	18 <sup>h</sup> 08 <sup>m</sup> 50 <sup>s</sup> .82	-27° 40' 12.''6	1.''00	4.7 <sup>+3.4</sup> <sub>-2.4</sub>	< 0.30
10	2.79	18 <sup>h</sup> 08 <sup>m</sup> 48 <sup>s</sup> .86	-27° 40' 34.''6	0.''97	5.7 <sup>+3.6</sup> <sub>-2.4</sub>	> -0.43
11	3.25	18 <sup>h</sup> 09 <sup>m</sup> 14 <sup>s</sup> .60	-27° 41' 03.''5	0.''79	24 <sup>+6</sup> <sub>-5</sub>	0.16 ± 0.28
12	3.50	18 <sup>h</sup> 09 <sup>m</sup> 10 <sup>s</sup> .00	-27° 44' 19.''9	1.''15	5.5 <sup>+3.6</sup> <sub>-2.4</sub>	< -0.08
13	3.52	18 <sup>h</sup> 08 <sup>m</sup> 47 <sup>s</sup> .45	-27° 43' 51.''1	1.''03	7.5 <sup>+4.0</sup> <sub>-2.8</sub>	< 0.11
14	3.54	18 <sup>h</sup> 08 <sup>m</sup> 49 <sup>s</sup> .93	-27° 44' 28.''1	1.''28	4.5 <sup>+3.4</sup> <sub>-2.2</sub>	< 0.33
15	3.61	18 <sup>h</sup> 09 <sup>m</sup> 14 <sup>s</sup> .30	-27° 43' 36.''4	1.''50	3.5 <sup>+3.1</sup> <sub>-2.2</sub>	< 0.33
16	4.02	18 <sup>h</sup> 08 <sup>m</sup> 53 <sup>s</sup> .34	-27° 38' 03.''3	1.''25	6.2 <sup>+3.8</sup> <sub>-2.6</sub>	-0.20 ± 0.71
17	4.05	18 <sup>h</sup> 08 <sup>m</sup> 57 <sup>s</sup> .42	-27° 37' 45.''8	1.''18	7.2 <sup>+4.0</sup> <sub>-2.8</sub>	0.24 ± 0.64
18	4.24	18 <sup>h</sup> 08 <sup>m</sup> 45 <sup>s</sup> .39	-27° 44' 26.''2	0.''87	23 <sup>+6</sup> <sub>-5</sub>	-0.36 ± 0.29
19	4.53	18 <sup>h</sup> 08 <sup>m</sup> 39 <sup>s</sup> .80	-27° 41' 31.''6	0.''74	230 <sup>+16</sup> <sub>-15</sub>	0.76 ± 0.09
20	4.67	18 <sup>h</sup> 09 <sup>m</sup> 20 <sup>s</sup> .65	-27° 42' 57.''5	1.''56	5.9 <sup>+3.8</sup> <sub>-2.6</sub>	-0.24 ± 0.75
21	6.24	18 <sup>h</sup> 09 <sup>m</sup> 28 <sup>s</sup> .33	-27° 41' 11.''9	2.''71	5.9 <sup>+4.0</sup> <sub>-2.8</sub>	< -0.07
22	6.25	18 <sup>h</sup> 09 <sup>m</sup> 00 <sup>s</sup> .14	-27° 48' 00.''9	1.''75	11 <sup>+3</sup> <sub>-4</sub>	-0.16 ± 0.49
23	6.30	18 <sup>h</sup> 08 <sup>m</sup> 56 <sup>s</sup> .93	-27° 48' 01.''5	2.''77	5.9 <sup>+4.0</sup> <sub>-2.8</sub>	-0.13 ± 0.77
24	6.76	18 <sup>h</sup> 08 <sup>m</sup> 30 <sup>s</sup> .22	-27° 40' 33.''0	2.''40	8.6 <sup>+4.0</sup> <sub>-2.8</sub>	> -0.10
25	7.40	18 <sup>h</sup> 09 <sup>m</sup> 00 <sup>s</sup> .16	-27° 49' 10.''3	1.''37	30 <sup>+7</sup> <sub>-6</sub>	-0.29 ± 0.26
26	7.60	18 <sup>h</sup> 08 <sup>m</sup> 36 <sup>s</sup> .70	-27° 47' 17.''8	3.''71	7.2 <sup>+4.6</sup> <sub>-3.5</sub>	> -0.21
27	7.72	18 <sup>h</sup> 08 <sup>m</sup> 30 <sup>s</sup> .25	-27° 45' 42.''7	2.''39	13 <sup>+3</sup> <sub>-4</sub>	0.17 ± 0.45
28	7.87	18 <sup>h</sup> 08 <sup>m</sup> 54 <sup>s</sup> .52	-27° 49' 32.''1	1.''91	20 <sup>+6</sup> <sub>-5</sub>	-0.25 ± 0.35
29	9.96	18 <sup>h</sup> 08 <sup>m</sup> 38 <sup>s</sup> .95	-27° 50' 32.''5	12.''77	4.5 <sup>+5.5</sup> <sub>-4.4</sub>	< 0.74
<b>IGR J18381-0924</b>						
1	1.84	18 <sup>h</sup> 38 <sup>m</sup> 02 <sup>s</sup> .02	-09° 23' 43.''9	0.''73	33 <sup>+7</sup> <sub>-6</sub>	0.70 ± 0.26
2	2.78	18 <sup>h</sup> 38 <sup>m</sup> 18 <sup>s</sup> .58	-09° 25' 52.''2	0.''70	303 <sup>+18</sup> <sub>-12</sub>	0.73 ± 0.08
3	2.82	18 <sup>h</sup> 38 <sup>m</sup> 20 <sup>s</sup> .11	-09° 23' 55.''6	1.''14	3.7 <sup>+1.2</sup> <sub>-1.2</sub>	< 0.54
4	3.63	18 <sup>h</sup> 38 <sup>m</sup> 15 <sup>s</sup> .91	-09° 27' 38.''9	1.''30	4.6 <sup>+3.4</sup> <sub>-2.4</sub>	< 0.61
5	3.76	18 <sup>h</sup> 38 <sup>m</sup> 16 <sup>s</sup> .55	-09° 21' 12.''6	1.''14	6.5 <sup>+3.3</sup> <sub>-2.2</sub>	< 0.00
6	4.14	18 <sup>h</sup> 38 <sup>m</sup> 22 <sup>s</sup> .64	-09° 22' 05.''8	0.''80	42 <sup>+8</sup> <sub>-7</sub>	> 0.58
7	4.27	18 <sup>h</sup> 37 <sup>m</sup> 51 <sup>s</sup> .59	-09° 24' 09.''6	1.''24	7.4 <sup>+4.0</sup> <sub>-2.8</sub>	< -0.10
8	5.72	18 <sup>h</sup> 37 <sup>m</sup> 59 <sup>s</sup> .66	-09° 29' 42.''5	1.''76	8.4 <sup>+4.0</sup> <sub>-2.8</sub>	> 0.13
9	6.14	18 <sup>h</sup> 38 <sup>m</sup> 30 <sup>s</sup> .63	-09° 27' 26.''9	1.''77	10 <sup>+3</sup> <sub>-3</sub>	< -0.11
10	6.46	18 <sup>h</sup> 38 <sup>m</sup> 07 <sup>s</sup> .59	-09° 18' 00.''3	3.''47	4.8 <sup>+3.8</sup> <sub>-2.6</sub>	< 0.25
11	6.49	18 <sup>h</sup> 38 <sup>m</sup> 33 <sup>s</sup> .67	-09° 26' 38.''1	2.''02	10 <sup>+3</sup> <sub>-3</sub>	-0.13 ± 0.52
12	7.51	18 <sup>h</sup> 38 <sup>m</sup> 17 <sup>s</sup> .63	-09° 31' 39.''2	2.''76	10 <sup>+3</sup> <sub>-3</sub>	-0.05 ± 0.54
13	8.16	18 <sup>h</sup> 37 <sup>m</sup> 50 <sup>s</sup> .30	-09° 17' 41.''9	1.''11	81 <sup>+10</sup> <sub>-9</sub>	0.01 ± 0.13
14	8.37	18 <sup>h</sup> 37 <sup>m</sup> 54 <sup>s</sup> .41	-09° 32' 01.''7	3.''24	11 <sup>+5</sup> <sub>-4</sub>	-0.25 ± 0.51
<b>IGR J20107+4534</b>						
1	1.40	20 <sup>h</sup> 10 <sup>m</sup> 43 <sup>s</sup> .20	+45° 34' 49.''6	0.''76	11 <sup>+4</sup> <sub>-3</sub>	-0.28 ± 0.47
2	1.44	20 <sup>h</sup> 10 <sup>m</sup> 30 <sup>s</sup> .05	+45° 34' 46.''7	0.''80	6.8 <sup>+3.8</sup> <sub>-2.6</sub>	< -0.19
3	2.12	20 <sup>h</sup> 10 <sup>m</sup> 48 <sup>s</sup> .95	+45° 34' 06.''5	0.''74	26 <sup>+6</sup> <sub>-5</sub>	< -0.66
4	2.87	20 <sup>h</sup> 10 <sup>m</sup> 20 <sup>s</sup> .61	+45° 33' 34.''7	1.''05	4.7 <sup>+3.4</sup> <sub>-2.4</sub>	> -0.66
5	3.63	20 <sup>h</sup> 10 <sup>m</sup> 47 <sup>s</sup> .47	+45° 30' 51.''2	1.''31	4.5 <sup>+3.4</sup> <sub>-2.4</sub>	> -0.11
6	3.69	20 <sup>h</sup> 10 <sup>m</sup> 34 <sup>s</sup> .82	+45° 37' 38.''3	1.''90	2.5 <sup>+2.9</sup> <sub>-1.7</sub>	< 0.77
7	4.14	20 <sup>h</sup> 10 <sup>m</sup> 25 <sup>s</sup> .50	+45° 37' 36.''1	1.''40	5.3 <sup>+3.6</sup> <sub>-2.6</sub>	> -0.49
8	4.30	20 <sup>h</sup> 10 <sup>m</sup> 12 <sup>s</sup> .27	+45° 33' 55.''6	1.''35	6.2 <sup>+3.8</sup> <sub>-2.6</sub>	-0.22 ± 0.71
9	4.54	20 <sup>h</sup> 10 <sup>m</sup> 52 <sup>s</sup> .12	+45° 30' 17.''8	0.''99	16 <sup>+5</sup> <sub>-4</sub>	< -0.49
10	4.74	20 <sup>h</sup> 10 <sup>m</sup> 26 <sup>s</sup> .36	+45° 38' 20.''4	3.''36	2.1 <sup>+2.9</sup> <sub>-1.7</sub>	—
11	5.20	20 <sup>h</sup> 10 <sup>m</sup> 56 <sup>s</sup> .40	+45° 37' 53.''7	1.''47	8.7 <sup>+4.3</sup> <sub>-3.1</sub>	-0.06 ± 0.55
12	5.63	20 <sup>h</sup> 10 <sup>m</sup> 27 <sup>s</sup> .57	+45° 28' 34.''4	1.''23	16 <sup>+5</sup> <sub>-4</sub>	< -0.51
13	7.48	20 <sup>h</sup> 11 <sup>m</sup> 19 <sup>s</sup> .30	+45° 34' 51.''8	1.''38	31 <sup>+7</sup> <sub>-6</sub>	0.10 ± 0.25

<sup>a</sup>The angular distance between the center of the *INTEGRAL* error circle and the source. In each case, the *INTEGRAL* error circle radius is 2.'1 at 1- $\sigma$  (Krivonos et al. 2012) and 4.'2 at 2- $\sigma$ .

<sup>b</sup>The 90% confidence uncertainty on the position, including statistical and systematic contributions.

<sup>c</sup>The number of ACIS-I counts detected (after background subtraction) in the 0.3–10 keV band. The errors are 68% confidence Poisson errors using the analytical approximations from Gehrels (1986).

<sup>d</sup>The hardness is given by  $(C_2 - C_1)/(C_2 + C_1)$ , where  $C_2$  is the number of counts in the 2–10 keV band and  $C_1$  is the number of counts in the 0.3–2 keV band.

TABLE 6  
POSITION SHIFTS BASED ON *Chandra*/NEAR-IR MATCHES

IGR Name	Near-IR Catalog	$N_{\text{matches}}^{\text{a}}$	R.A. shift	Decl. shift
J14091–6108	VISTA/VVV	10	+0.''01	+0.''23
J15335–5420	VISTA/VVV	5	–0.''01	–0.''25
J17164–3803	VISTA/VVV	5	–0.''43	–0.''20
J17174–2436	UKIDSS	1	—	—
J17306–2015	2MASS	2	—	—
J18088–2741	VISTA/VVV	15	–0.''09	+0.''09
J18381–0924	UKIDSS	3	—	—
J20107+4534	2MASS	5	–0.''29	–0.''29

<sup>a</sup>The number of matches between *Chandra* sources and sources in the near-IR catalog after running `wcs_match`.